

Probing Axial Symmetry Breaking in the Galaxy with Gaia Data Release 2

Austin Hinkel¹, Susan Gardner¹, and Brian Yanny²

Department of Physics and Astronomy, University of Kentucky, Lexington, KY 40506-0055, USA

Fermi National Accelerator Laboratory, Batavia, IL 60510, USA

Received 2019 December 23; revised 2020 March 3; accepted 2020 March 18; published 2020 April 21

Abstract

We study a set of solar neighborhood (d < 3 kpc) stars from Gaia Data Release 2 to determine azimuthal star count differences, i.e., left and right of the line from the Galactic Center (GC) through the Sun—and compare these differences north and south. In this companion paper to Gardner et al., we delineate our procedures to remove false asymmetries from sampling effects, incompleteness, and/or interloper populations, as this is crucial to tests of axisymmetry. Particularly, we have taken care to make appropriate selections of magnitude, color, in-plane Galactocentric radius, and Galactic |b| and |z|. We find that requiring parallax determinations of high precision induces sampling biases, so that we eschew such requirements and exclude, e.g., regions around the lines of sight to the Magellanic Clouds, along with their mirror-image lines of sight, to ensure well-matched data sets. After making conservative cuts, we demonstrate the existence of azimuthal asymmetries and find differences in those, north and south. These asymmetries give key insights into the nature and origins of the perturbations on Galactic matter, allowing us to assess the relative influence of the Magellanic Clouds (LMC and SMC), the Galactic bar, and other masses on the Galactic mass distribution, as described in Gardner et al. The asymmetry's radial dependence reveals variations that we attribute to the Galactic bar, and it changes sign at a radius of $(0.95 \pm 0.03)R_0$, with R_0 the Sun–GC distance, to give us the first direct assessment of the outer Lindblad resonant radius.

Unified Astronomy Thesaurus concepts: Milky Way dark matter halo (1049); Milky Way Galaxy (1054); Galaxy structure (622); Milky Way dynamics (1051)

1. Introduction

Models of the Galaxy are often motivated by the assumption that it is isolated and thus has certain integrals of motion. It is, moreover, commonly regarded as a superposition of its disk, halo, bulge, and bar components (Robin et al. 2003, 2012). Each component i can be modeled by a distribution function f_i (Binney & Tremaine 2008; Binney 2012; Bovy & Rix 2013; Piffl et al. 2014, 2015), which, in steady state, is characterized by its integrals of motion, as predicated by Jeans' theorem (Jeans 1915). It is useful to model $f_i(\mathbf{J})$, where \mathbf{J} has as components the action integrals J_r , J_ϕ , and J_z , in radial, azimuthal, and vertical coordinates r, ϕ , and z with respect to the plane of the Galactic disk. Notably J_{ϕ} (or " L_z ") is the angular momentum about the symmetry axis of an axisymmetric disk. Each $f_i(J)$ is a supposed invariant under the slow evolution of the Galaxy. Although the Galaxy has features that are notably axially asymmetric, namely, the spiral arms and Galactic bar, it is nevertheless the case that f(J) modeling (Binney et al. 2014) gives a very good description of the velocity distributions observed by the RAVE survey. With the advent of Gaia Data Release 2 (DR2) data (Prusti et al. 2016; Lindegren et al. 2018) it has become possible to determine the structure of the dark halo from the stars alone (Binney & Piffl 2015), in that the circular speed curve with the in-plane Galactic radius R from the reconstructed Galactic potential is compatible with the circular speed from Cepheids (Binney 2019; Mróz et al. 2019).

An integral of motion used to model the Galactic distribution function should also correspond to a continuous symmetry, as the converse of Noether's Theorem (Noether 1918) holds if the integral of motion is nonzero (Olver 1993). Thus, in regions nominally described by just a disk and spheroidal halo, we expect the angular momentum about the z-axis, L_z , to be an

integral of motion and thus axial symmetry should be manifest. However, we know structures such as the Galactic bar and spiral arms do not exhibit axial symmetry, and there are also satellite galaxies that may influence the Milky Way. It is thus interesting to assess the degree to which the Galaxy is truly axisymmetric away from these known asymmetric sources, as doing so can provide insights into the validity of the above assumptions and help to determine which perturbers may be most relevant.

In practice, to test axial symmetry, one simply needs to count the stars in a given range of Galactocentric longitude, ϕ , and then compare the counts of that bin with the bin corresponding to a Galactocentric longitude range that has been reflected across the $\phi = 180^{\circ}$ line. With the star counts of the left $(n_{\rm L}, \phi > 180^{\circ})$ and right $(n_{\rm R}, \phi < 180^{\circ})$ bins, one is able to compute the asymmetry, as defined in Gardner et al. (2020):

$$\mathcal{A}(\phi) = \frac{n_{L}(\phi) - n_{R}(\phi)}{n_{L}(\phi) + n_{R}(\phi)},\tag{1}$$

where the functions $n_{\rm L,R}$ (ϕ) contain integrals over the other coordinates as appropriate. Computing axial asymmetries for the Galaxy would, in theory, be possible with respect to any Galactocentric longitude, but due to observational constraints driven by the heliocentric nature of our $|b| > 30^{\circ}$ latitude cuts and the limited reach of the Gaia telescope, we use the $\phi = 180^{\circ}$ line as our baseline and limit our probe to Galactocentric longitudes within 6° of this baseline and within Galactocentric in-plane distances of 7 < R < 9 kpc, where the Sun is assumed to be at $R = R_0 = 8$ kpc, though we note the recent result of 8.178 ± 0.026 kpc from Abuter et al. (2019), and vertical distances of no more than 3 kpc above or below the plane. A schematic depiction of the (in-plane projected) geometry involved in this process can be found in Figure 1.

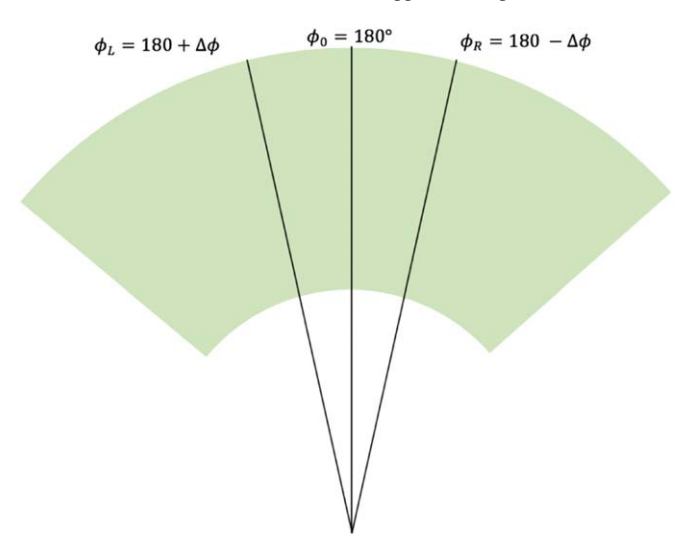


Figure 1. A schematic depiction (i.e., not to scale) of the method of computing an axial asymmetry. To construct $\mathcal{A}(\phi)$, one counts the number of stars, $n_{\rm R}$, in a range $\delta\phi$ about an angle $\phi_{\rm R}$ to the right of the $\phi=180^\circ$ line, that is, in a bin centered on $\phi_{\rm R}$, and then counts the number of stars, $n_{\rm L}$, in a bin of width $\delta\phi$ centered on the angle $\phi_{\rm L}$ to the left of the $\phi=180^\circ$ line, chosen such that $\phi_{\rm L}=180^\circ+\Delta\phi$, where $\phi_{\rm R}=180^\circ-\Delta\phi$ and $\Delta\phi>0$. The asymmetry can be computed from $n_{\rm L,R}$ via Equation (1). Note we choose uniform bins in $\delta\phi$ across the region of interest, so that we can assess $A(\phi)$ with ϕ .

If tests of axial symmetry about other "fold" lines were ever to become practicable, our ability to probe dynamical effects, such as from the presence of the Galactic bar, would be greatly heightened.

To our knowledge, a test of axial asymmetry in stars out of the Galactic midplane region is first employed in Gardner et al. (2020). In this companion paper we carefully develop the data selection procedures that make the studies of Gardner et al. (2020) possible. There we concluded that significant asymmetries in the left versus right star counts combined with north and south subcounts clearly imply the influence of massive objects that break the axial symmetry of the Milky Way's stellar and overall matter distributions. Comparing the relative torques due to well-known "perturber" candidates, we found the influence of the LMC to be dominant. However, due to uncertainties in the mass distributions, including those from unseen dark matter, we could not rule out that some fraction of the mismatch in counts left and right and north and south could be due to other structures, such as the Sagittarius (Sgr) dwarf tidal stream and the Galactic bar. Gardner et al. (2020) were further able to distinguish between oblate and prolate mass distributions by looking at not only "global" several degree scale (in ϕ) axial asymmetries, but also how these asymmetries differed north and south of the midplane. In Gardner et al. (2020) we considered the analysis volume we develop in this paper, namely, the selection 7 < R < 9 kpc, 0.2 < |z| < 3 kpc, $|b| > 30^{\circ}$ as a whole, along with brightness and color selections and particular sight-line exclusions. Here, we subdivide the data further in an attempt to find out if the LMC is responsible for the entirety of the asymmetries, and we discover important asymmetric effects from the Galactic bar. In what follows we carefully delineate our data selection and analysis procedures before turning to a discussion of the axial asymmetries, in aggregate and in various subspaces of our analysis data set.

2. Data Selection and Completeness Studies

The Gaia documentation and supporting publications (Bailer-Jones 2015; Luri et al. 2018) suggest using a Bayesian approach to estimate distances, particularly if the relative errors in parallax are large. We do not use such an approach here, as we do not need to know a precise distance to a star, just the correct azimuthal bin into which it falls. Thus we estimate the distance to each object as the inverse of its parallax, ϖ , throughout. Additionally, we do not see any evidence that the measured parallaxes are systematically correlated with a star's location left or right of the $\phi=180^\circ$ line.

As noted by Luri et al. (2018), using small relative parallax error quality cuts introduces artificial asymmetries, or biases, into a data set, because the parallax error is a function of position on the sky due to the Gaia scanning law's nonuniform sampling of different regions of the sky. This would irreparably bias the study of symmetries over an appreciable extent of the Galaxy, as shown in Figure 2(a). Instead, we outline here a method for selecting a set of stars that appears to be free of any obvious biases (Figure 2(b)) and is smoothly distributed in multiple parameter spaces, indicating that no chunks of data are missing or significantly afflicted by observational biases. To wit, we use the photometric and astrometric data to effect cuts that preserve a smooth distribution of stars in G-band magnitude, $G_{\rm BP}-G_{\rm RP}$ color, in-plane radius from the Galactic Center (GC), and height above the plane over a range of Galactocentric longitudes centered on the anticenter line, $\phi = 180^{\circ}$. The logic of the alternative method we propose is as follows: if there is an artificial bias in the Gaia data set, it would manifest itself as some aberration from the expected smoothly varying distributions in at least one parameter space. In the subsections that follow, we outline each parameter space checked and use the plots generated in this study to motivate a maximal angular reach to which we can safely test axial symmetry with strong statistics.

2.1. Data Acquisition

The relevant data for this analysis were obtained from the European Space Agency's Gaia space telescope (Prusti et al. 2016), via the online archive.³ Selections were made in windows of (l, b) with $\varpi_{\text{unshifted}} > -0.07$ mas and $|b| > 30^{\circ}$. The latter cut is made in order to stay above the dust and gas close to the midplane while the former was made so that after a global shift of 0.07 mas is applied to the parallax, we have only stars with physical parallaxes, so that in the shifted parallax, $\varpi > 0$ mas. We assume this shift in all that follows. The particular value for the parallax zero-point shift was chosen from a wide array offered in the literature (Lindegren et al. 2018; Stassun & Torres 2018; Zinn et al. 2019) such that our value is a "middle-ground" choice. The particular choice of shift has no bearing on the final results as our data are quite close (the mean distance to a star in our sample is 0.94 kpc, with $\sim 60\%$ of the stars within 1 kpc), and thus do not bring previously negative parallaxes into the analysis. Additionally, our analysis requires that a distance estimate via a parallax is available, so that we use only data for which the full fiveparameter astrometric solution is available, as the twoparameter solution does not specify a distance (Luri et al. 2018). After the analysis of the following two subsections, we

https://gea.esac.esa.int/archive/

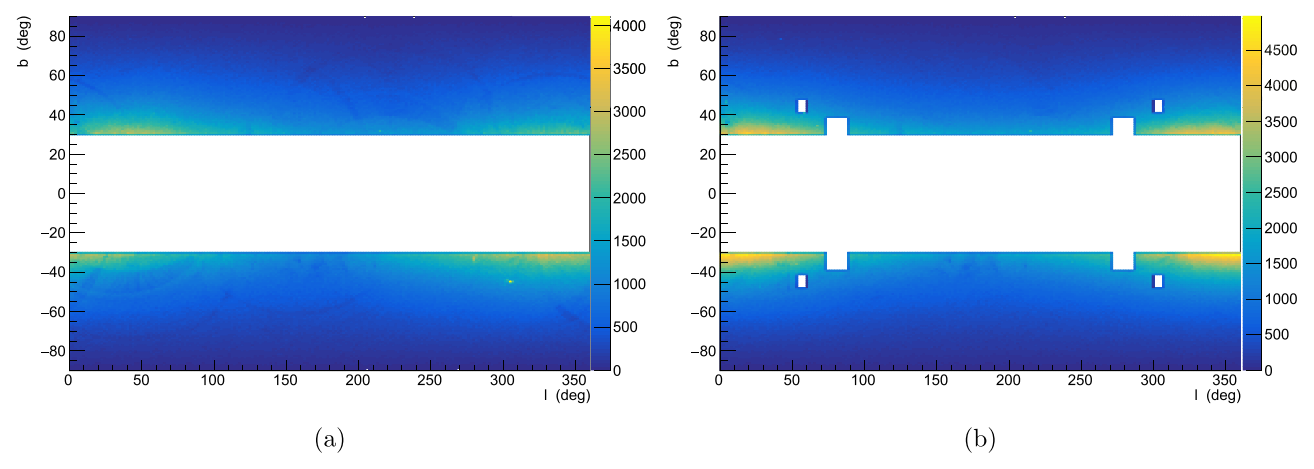


Figure 2. (a) A selection of data in (l, b) with relative parallax error cuts of $\sigma_{\varpi}/\varpi < 0.2$ applied. Notice the LMC and SMC "bleed" through, even though their stars are at significantly greater distances than expected from a simple lower limit cut on the parallax with its error; stellar identification issues in the crowded field may be the cause of this issue. There are also streaks of incompleteness in the data, a sign that Gaia did not measure stars in some regions of the sky with the same accuracy as others. (b) A selection of data in (l, b) with the LMC and SMC removed, as well as all reflections of the two satellite galaxies to prevent any bias in an assessment of left/right and north/south symmetry. The cuts used are as follows: 14 < G < 18 mag, $0.5 < G_{BP} - G_{RP} < 2.5$, $\varpi > 0$ mas, $|b| > 30^\circ$, 0.2 < |z| < 3 kpc, and the LMC/SMC excisions as outlined in Equations (2) and (3). We note that some dust seems to survive the |b| and |z| cuts near the anticenter direction. We have checked our final result with and without excisions of this region and there appears to be no appreciable effect.

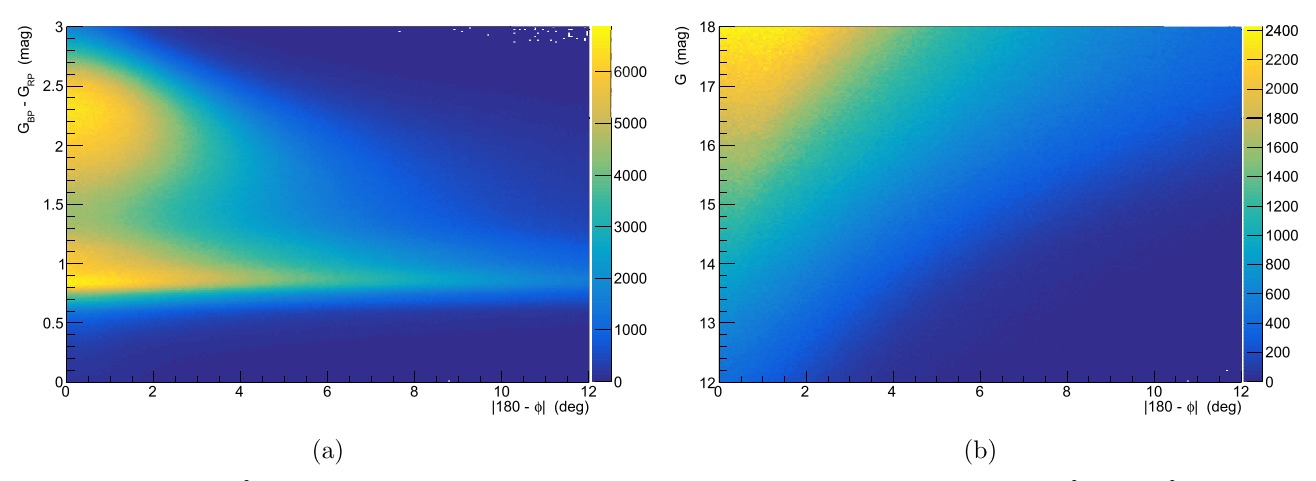


Figure 3. (a) $G_{\rm BP}-G_{\rm RP}$ vs. $|180^\circ-\phi|$. For $0.5 < G_{\rm BP}-G_{\rm RP} < 2.5$ there appears to be significant statistical strength out to $|180^\circ-\phi|\approx 6^\circ$. The cuts used are as follows: $\varpi>0$ mas, $|b|>30^\circ$, and the LMC/SMC excision outlined in Equations (2) and (3). We note that the final results do not change appreciably upon changing the color cut from $G_{\rm BP}-G_{\rm RP} < 2.5$ mag to $G_{\rm BP}-G_{\rm RP} < 2.3$ mag. (b) $G_{\rm BP}-G_{\rm RP} < 2.5$ mag, $G_{\rm BP}-G_{\rm RP} < 2.5$ ma

conclude that elimination of the stars with the two-parameter "fall-back" solution does not bias our result.

2.2. Masking Toward Select Anomalous Lines of Sight

In order to ensure our sample is not biased in the north versus south or for $\phi > 180^\circ$ or $\phi < 180^\circ$, we are forced (see below) to cut out the Large and Small Magellanic Clouds, as well as their reflections across the midplane, the reflections across the anticenter line, and the reflections across both the midplane and anticenter line, as in Figure 2(b). We note here that we choose not to apply relative parallax error quality cuts as suggested by Luri et al. (2018), as it is clear from Figure 2(a) that such cuts actually fail to remove the LMC and SMC from the data. Additionally, visible streaks appear in the completeness data if we apply these parallax error cuts, preventing an unbiased assessment of axial symmetry.

The excision of the LMC and SMC was checked in a series of (l,b) plots with the G, $G_{\rm BP}-G_{\rm RP}$, |b|, and |z| restrictions outlined below already in place. Thus, these selections act as an effective distance cut, which helps with the elimination of the LMC/SMC contamination caused by poor parallax assessments in the dense field. The LMC and SMC sight lines, along with the appropriate reflections we have mentioned, are removed by excising all the data that fit the following criteria:

$$|b| \in [30^{\circ}, 39^{\circ}] \land (l \in [271^{\circ}, 287^{\circ}] \lor l \in [73^{\circ}, 89^{\circ}])$$
 (2)

and

$$|b| \in [41^{\circ}, 48^{\circ}] \land (l \in [299^{\circ}, 307^{\circ}] \lor l \in [53^{\circ}, 61^{\circ}])$$
 (3)

for the LMC and SMC, respectively.

Although some dust seems to survive our |b| and |z| cuts in the region beyond the Sun's radius, we have checked that our

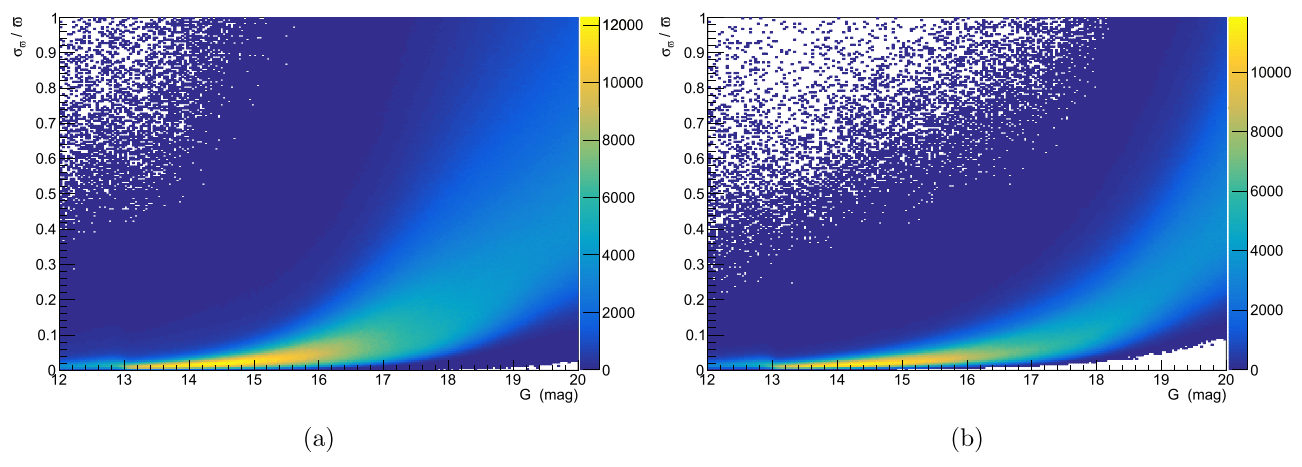


Figure 4. (a) The majority of stars with magnitude G have a relative parallax error that is reasonably small for G < 18 mag. The Gaia documentation mentions incompleteness in crowded fields and due to data processing and "filtering" for stars with G > 17 mag in crowded regions (Arenou et al. 2018); however, we avoid these regions and can thus extend our reach to fainter stars, as motivated in the text. The cuts used are as follows: $0.5 < G_{\rm BP} - G_{\rm RP} < 2.5$ mag, $\varpi > 0$ mas, $|b| > 30^\circ$, and the LMC/SMC excision outlined in Equations (2) and (3). These are the "standard cuts" that we employ throughout our analysis. (b) The relative error in the parallax for our selection of stars, though without G restrictions. We manage to select stars with relatively well-measured parallaxes without incurring the bias of cutting on relative parallax error explicitly. The cuts used are as follows: $0.5 < G_{\rm BP} - G_{\rm RP} < 2.5$ mag, $\varpi > 0$ mas, $|b| > 30^\circ$, 7 < R < 9 kpc, and the LMC/SMC excision outlined in Equations (2) and (3).

asymmetry results do not change appreciably if that region is excised from our data set.

In order to assess the completeness of our sample after the implementation of the above "box" cuts, the distribution of stars with respect to the angle $|180^{\circ} - \phi|$ was examined for multiple different parameters. Beginning with the color and G-band magnitudes of our sample, as depicted in Figures 3(a) and (b), respectively, we see that there are various ranges of both parameters where we simply lack enough stars to probe very far from the $\phi=180^{\circ}$ line. In the interest of obtaining both a large number of stars and a nonnegligible reach in $|180^{\circ} - \phi|$, we choose to keep stars for which $G_{\rm BP} - G_{\rm RP} \in [0.5, 2.5]$ mag and $G \geqslant 14$ mag. We also note that the distribution shows no signs of any obvious incompleteness.

2.3. Limits on G Magnitude, $G_{BP} - G_{RP}$ Color, R, and |z|

Although Figure 3(b) suggests that one may probe larger values of $|180^{\circ} - \phi|$ for fainter stars, one runs into unreliable parallax measurements for G > 18 mag, as the majority of stars in the trend from Figure 4 with G > 18 mag have $\sigma_{\varpi}/\varpi > 0.2$. As such, we consider only the window $G \in [14, 18]$ mag. While similar to the suggestion of Luri et al. (2018) that relative parallax error cuts be used, we instead rely on the magnitude as a rough proxy for the relative parallax error. Because we are looking away from the gas and dust of the plane due to our requirement that $|b| > 30^{\circ}$, we expect that the magnitudes observed by Gaia will not dramatically fluctuate over small scales like a hard cut on σ_{ϖ}/ϖ did in Figure 2(a). We are mindful that Luri et al. (2018) suggest cutting out all stars with G > 17 mag due to incompleteness in crowded fields, the scan-law pattern, and filtering during the data reduction process. We show later in Figure 12 that the quantitative result found for the smaller, recommended magnitude window is not very different than the $G \in$ [14, 18] mag window result. Since we have cut out the regions with crowding issues (i.e., low latitudes and the LMC and SMC), using G < 18 mag appears to be a valid option for our particular set of cuts. By using this faintness limit, we are adding statistical strength to our analysis.

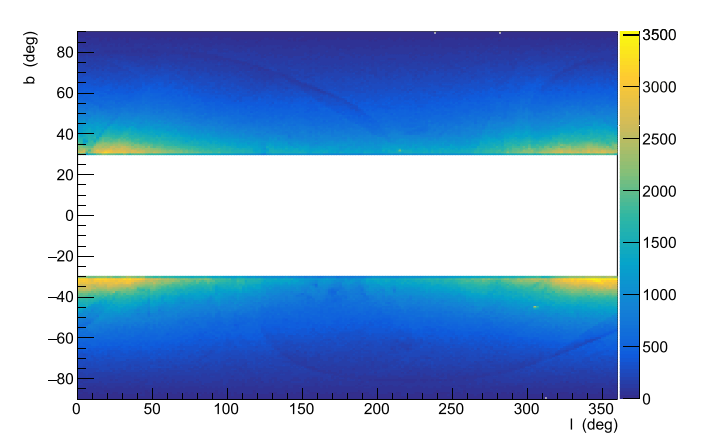


Figure 5. A study of stars within $\lesssim 3$ kpc with $|b| > 30^{\circ}$ and $G \in [14, 18]$ mag, but with restrictions on Astrometric Excess Noise (AEN) in place. All stars with an AEN value larger than 0.2 mas have been excised. Clearly, requiring such a quality cut would leave the sample with artificial asymmetries due to the streaks seen in many portions of the sky.

One possible alternative is using the Astrometric Excess Noise (AEN), available in the Gaia data (Lindegren et al. 2012), rather than the relative error in parallax, as it is not explicitly a function of the number of observations (Lindegren et al. 2018), which are known to be different in different parts of the sky (Lindegren et al. 2018). However, as Figure 5 illustrates, there is a significant bias incurred from restricting the values of the AEN. As such, we forgo any restrictions on the AEN, and instead check that our final data set results in a relatively small average AEN. For our particular latitudes, the mean AEN, (AEN), is about 1.034 mas for the entire Gaia database, whereas a similar yet slightly larger volume of space to our analysis (i.e., $\varpi > 0.3$ mas and $|b| > 30^{\circ}$) with stars having similar magnitudes and colors yields an upper bound value of $\langle AEN \rangle \approx 0.141$ mas, nearly an order of magnitude better.

Additionally, the distribution of our data set is checked over a range of in-plane radius, R, in Figure 6(a). From this examination, we cut on $R \in [7, 9]$ kpc in order to circumvent

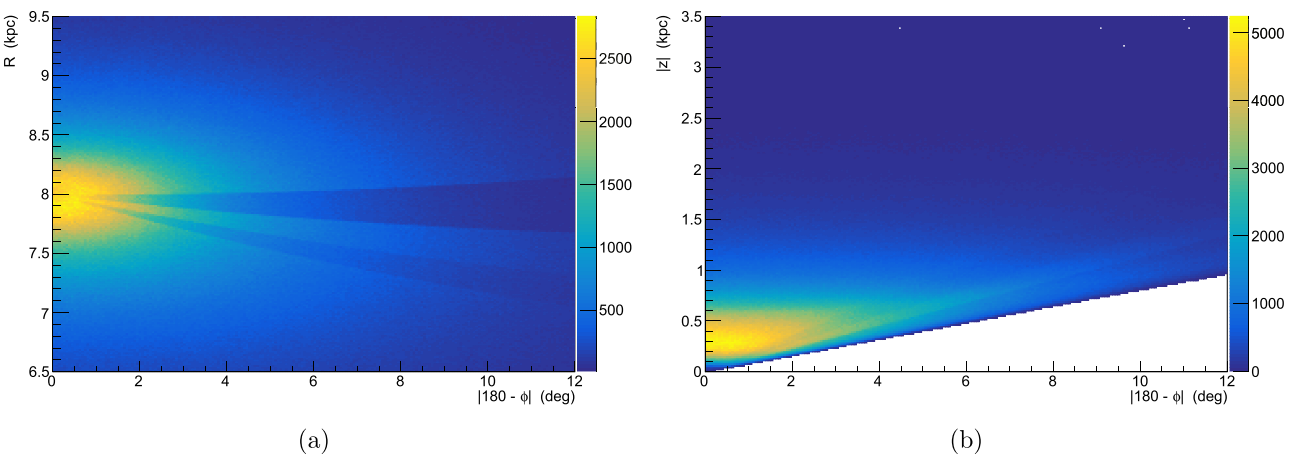


Figure 6. (a) R, ϕ completeness for the selected data. We choose to cut on 7 < R < 9 kpc in order to achieve the best angular reach possible without compromising completeness. The cuts used are as follows: 14 < G < 18 mag, $0.5 < G_{\rm BP} - G_{\rm RP} < 2.5$ mag, $\varpi > 0$ mas, $|b| > 30^{\circ}$, and the LMC/SMC excision outlined in Equations (2) and (3). (b) Test of vertical completeness over ϕ . Cuts used: 14 < G < 18 mag, $1.5 < G_{\rm BP} - G_{\rm RP} < 2.5$ mag, 7 < R < 9 kpc, $\varpi > 0$ mas, and the LMC/SMC excision outlined in Equations (2) and (3).

sampling a region of low statistical strength. To avoid the stars too close to the plane with known axially asymmetric features (e.g., spiral arms), we make a cut of |z| > 0.2 kpc. Also, to avoid straying too far from the disk into incomplete regions of |z|, we require |z| < 3 kpc as motivated by Figure 6(b), where we admittedly push the data set to its limits in order to sample more halo stars.

With all of the above constraints applied, we are left with a data set that is free of artificial biases left and right of the $\phi=180^\circ$ line. Not only is the data set well matched, the stars themselves are, on average, very well measured with a mean relative uncertainty in parallax of about 8.6% (see Table 1 for relative uncertainty in parallax for each quadrant). In order to visualize this resulting data set, we show the in-plane projection of our data in Figure 7(a). The geometry of the data in the R-|z| plane, on the other hand, is depicted in Figure 7(b). Figures 7(c) and (d) show the in-plane reach for red and blue stars, respectively, where one can see that the maximal reach in $|180^\circ - \phi|$ is reduced slightly for the redder population.

2.4. Consideration of Systematics

In order to assess the impact of various systematic effects on our data, we explore a number of different possibilities and estimate the degree to which they could cause a false asymmetry signal. First, due to the fact that we use Galactic azimuth values for each star, this necessitates that a parallax and thus a distance is known for the star. As such, this requirement eliminates all sources in the Gaia database that have a 2D "fall-back" astrometric solution only. Further, as we require color cuts for the completeness arguments we have outlined, we also miss stars with null entries for $G_{\rm BP}-G_{\rm RP}$. We have explicitly checked via a statistical query of the Gaia database that the asymmetry such an effect could cause would be $|A_{\text{null }\varpi} \& \text{ color}| \approx 0.0017$ for our G and |b| requirements. However, the preponderance of these stars lies outside our sample volume. Indeed, in a Bayesian analysis to associate a distance with the 2D fall-back solution, a prior used for the stars with poor astrometric measurements assumes a small parallax (Michalik et al. 2015), and therefore a large distance. Moreover, as we discuss further below, a Hubble Space Telescope comparison study suggests our sample is essentially

	Left	Right	Total
North	0.101	0.074	0.087
South	0.072	0.098	0.085
Total	0.086	0.086	0.086

Note. After applying the standard set of cuts enumerated in Figure 4 with $R \in [7, 9]$ kpc and $z \in [0.2, 3]$ kpc—and as also employed in Gardner et al. (2020).

100% complete. Therefore, the value given above is a gross overestimate, and taking the estimated incompleteness conservatively into account suggests that the estimated size of this systematic effect is no more than $|\mathcal{A}| \sim 2 \times 10^{-4}$.

Next, it is a well-known feature of the Gaia telescope that its orbital motion corresponds to certain parts of the sky being imaged more than others (Lindegren et al. 2018), hence the streaks seen when relative parallax error restrictions are made (Luri et al. 2018). However, this discrepancy in the number of observations does not affect whether or not a relatively close star is seen at all. In fact, the completeness of the Gaia data for relatively close stars has been checked against 2MASS and has been found to be about 99% complete for data selections not too dissimilar from ours (Bennett & Bovy 2018).

Further, the completeness of the Gaia data has been checked against the Hubble Space Telescope for dense fields in Arenou et al. (2018) and, for the range of magnitudes and latitudes considered here, is essentially 100% complete. In other words, by cutting away the densest regions of the sky and the dimmest stars, we are not affected by the completeness issues that often plague stars with such parameters.

Although the average angular densities considered in our analysis are all well within the range of safe values suggested by Arenou et al. (2018), one might worry that very localized lines of sight could exceed these density limits and result in small incomplete regions. We explicitly check this by zooming into the distribution of stars in l, b to search for small overdensities. We do find such regions, but we estimate that the impact of the stars missed in such cases on \mathcal{A} to be extremely

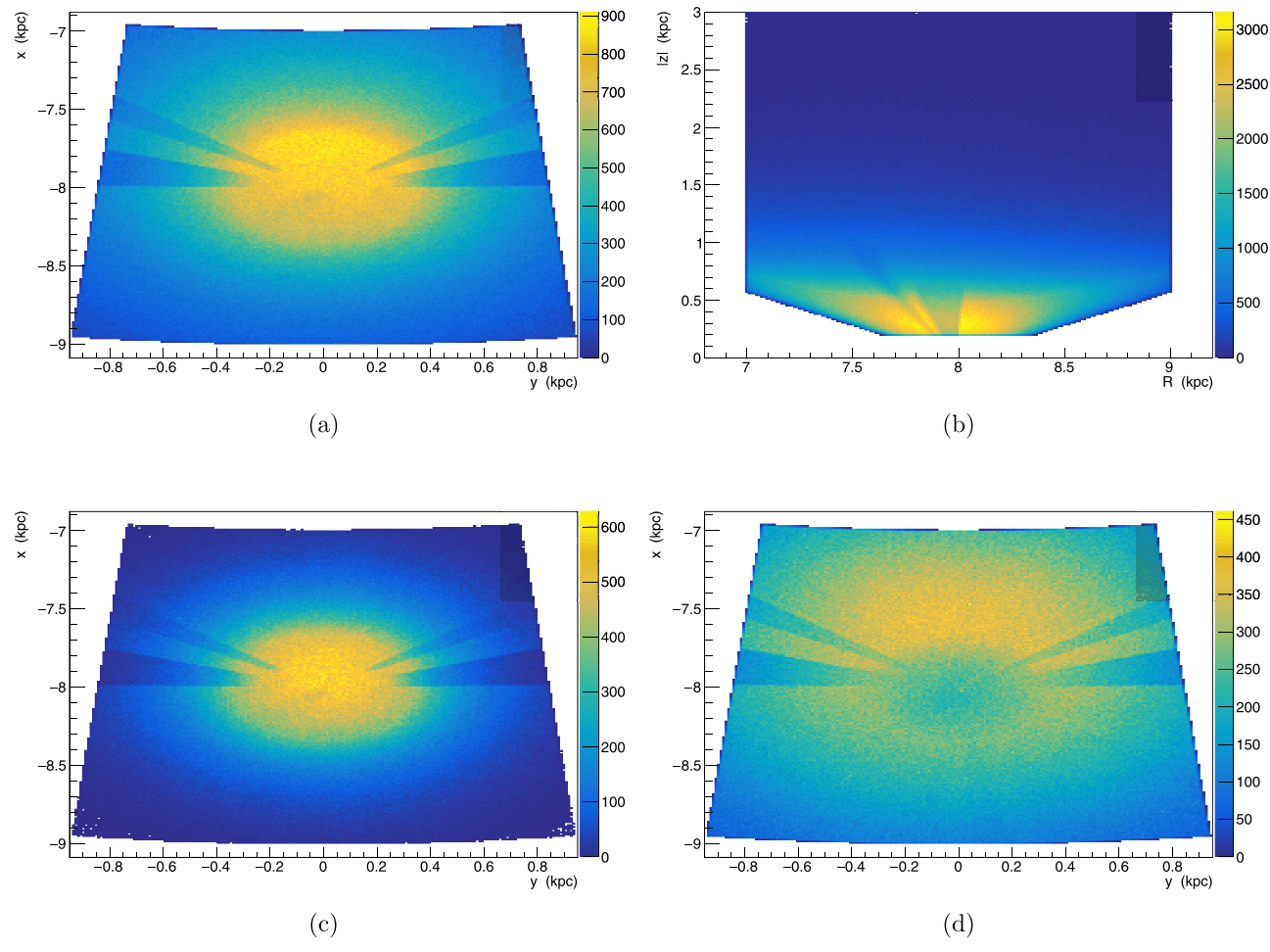


Figure 7. (a) The in-plane projection of our data with the cuts motivated above, as viewed from the south side of the plane. The data extend out to 6° in Galactocentric azimuth. (b) The geometry of our data selection in the R-|z| plane. (c) The in-plane projection for red stars $(1.5 < G_{\rm BP} - G_{\rm RP} < 2.5 \text{ mag})$. (d) The in-plane projection for blue stars $(0.5 < G_{\rm BP} - G_{\rm RP} < 1.5 \text{ mag})$. All panels have the following cuts unless noted otherwise: $0.5 < G_{\rm BP} - G_{\rm RP} < 2.5 \text{ mag}$, 14 < G < 18 mag, 14 <

small. We study a worst-case scenario by studying stars near $|b| = 30^{\circ}$ near the GC, gauging the expected level of completeness as detailed by Arenou et al. (2018). We find very localized areas with source densities near 4×10^{5} stars per square degree. Such a missing population of stars cannot possibly account for the symmetry breaking we see, as simply counting the overdense regions on each side of the $\phi = 180^{\circ}$ line yields an estimated asymmetry of $|\mathcal{A}| \approx 0.000013$.

Another possible systematic comes from the parallax offset. To first order, the parallax offset is assumed to be the same for stars in all directions, magnitudes, colors, etc. As such, there would be no differences left or right, and thus no contribution to the asymmetry. If instead the shift varies slightly on the sky, a small, $\mathcal{O}(0.01)$ mas correction to nearby stars would correspond to a distance shift of about 10 pc, or about 1% of the typical distance to a star in our sample. If this effect were truly an issue, the completeness checks we have performed would likely have exhibited some sort of noticeable fluctuation as stars with a different, true offset would have shifted into or out of our sample; we see no evidence of this.

Finally, the Gaia data obviously exhibit scan lines when relative parallax uncertainty quality cuts are implemented, so that one may be tempted to think that scan lines may also be hidden in the completeness plots at a level not detectable to the

human eye. To test this possibility, a number of tests were devised. First, upon zooming into small regions of l,b in our data where there are known streaks of incompleteness in the separate, relative parallax error data, as in Figure 2(a), we see no signs of any scan lines. Further, we numerically test this possibility by examining the expected asymmetry in our data set along the lines of sight toward a known streak in the relative parallax error data. The local, worst-case asymmetry is $|\mathcal{A}|=0.007$, and since the "would-be" streaks constitute a small fraction of the sky and are on both sides of the $\phi=180^\circ$ line, the expected, total asymmetry from any such effect is smaller still, perhaps something like a tenth of the worst-case local measurement, $|\mathcal{A}|=0.0007$.

Tallying the impact of the various systematic effects we have considered we estimate the total systematic error to be no larger than $|\mathcal{A}_{sys}| \sim 0.0009$. We note that this is substantially smaller than the asymmetry effects we have observed.

2.5. Splitting the Sample into Three Radial Bins

Since Gardner et al. (2020) studied the axial asymmetries for our aggregate sample and argued for a dominant role by the LMC and SMC in interpreting the results seen, we first split the sample into three R bins, 7 < R < 7.7, 7.7 < R < 8.3, and 8.3 < R < 9.0 kpc, in order to see if the asymmetry is constant

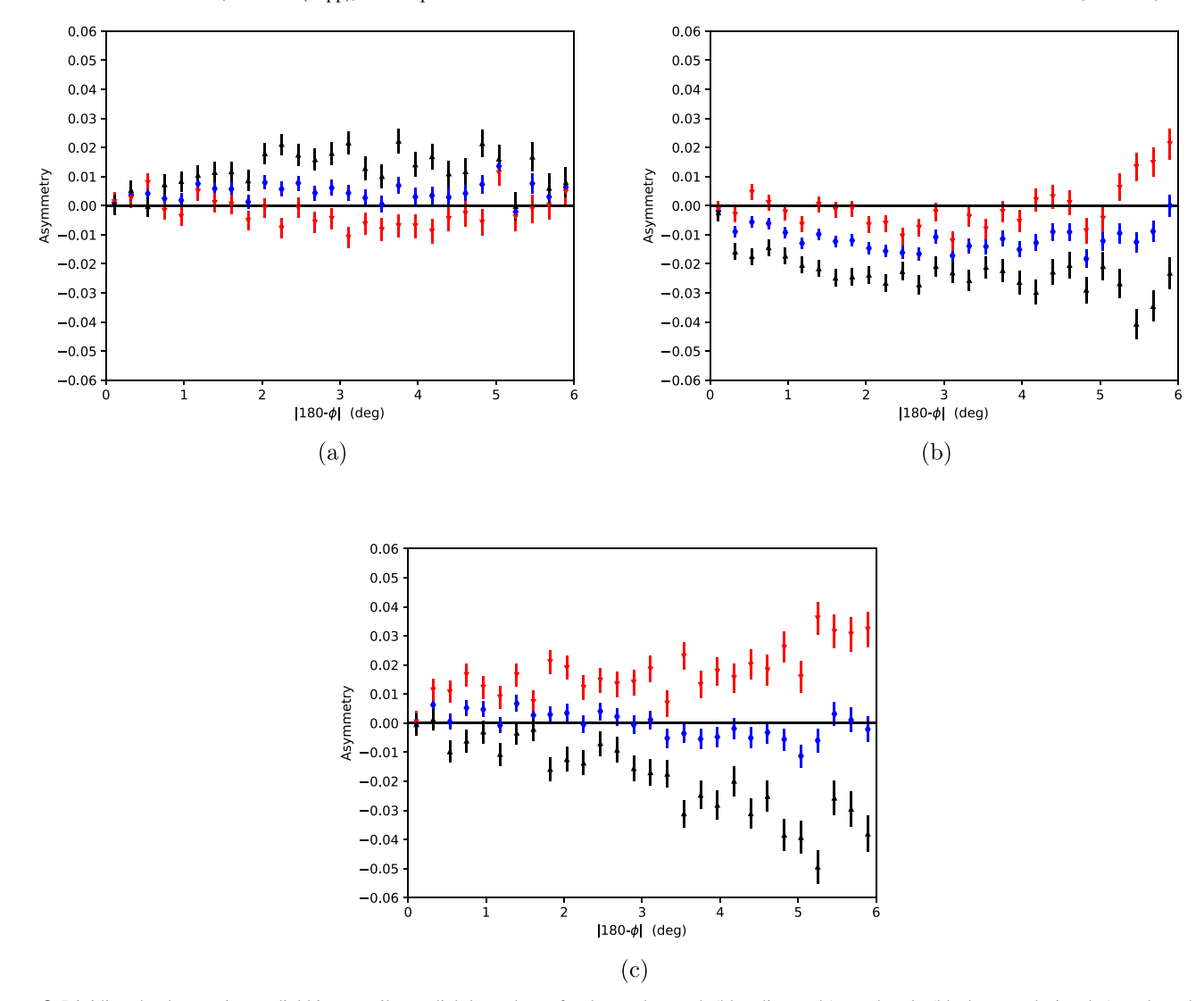


Figure 8. Dividing the data set into radial bins unveils a radial dependence for the north+south (blue diamonds), north only (black upward triangles), and south only (red downward triangles) asymmetries. (a) The axial symmetry test for stars with $R \in [7, 7.7]$ kpc. (b) The axial symmetry test for stars with $R \in [7.7, 8.3]$ kpc. (c) The axial symmetry test for stars with $R \in [8.3, 9]$ kpc. Additional cuts used in all panels are: $0.5 < G_{\rm BP} - G_{\rm RP} < 2.5$ mag, 14 < G < 18 mag, $\varpi > 0$ mas, $|b| > 30^{\circ}$, 0.2 < |z| < 3.0 kpc, $|180^{\circ} - \phi| \le 6^{\circ}$, and the LMC/SMC excision outlined in Equations (2) and (3).

with R. If the asymmetry were due entirely to the LMC, which because of its distance, would act over a relatively large coherent area of mass in the Milky Way, we would expect the A trends with ϕ to be similar in the three bins. Perhaps surprisingly, after dividing the sample into three radial bins, one instead notices marked differences in the shapes of the various asymmetry curves in Figure 8 with ϕ . These marked differences can potentially be understood as a superposition of two effects. First, given that the disk scale length is $R_s \approx 2 \,\mathrm{kpc}$ (Bovy & Rix 2013), the contribution of the halo to the total, north+south asymmetry (blue diamonds) is less pronounced in the inner region with more disk stars. The second effect we resolve is in only the two lowest R bins. In the innermost case, the left-heavy asymmetry differs in sign from the model matter distribution with a distorted halo (Erkal et al. 2019) that can confront the shape of the aggregate data fairly well (Gardner et al. 2020). Interestingly, such an R variation in the asymmetry could qualitatively be an expected signal from an outer Lindblad resonance (OLR) of the Galactic bar, where we note Figure 1 of Dehnen (2000) and the explanations of Contopoulos & Papayannopoulos (1980), or perhaps the corotation resonance

(CR) of the Galactic bar—as we discuss further below. Given that such effects are not axially symmetric, our method is sensitive to them and thus we may be able to discriminate between these two possibilities.

2.6. Masking out the GC and Removing Dimmer Stars

Given that the GC direction has an extremely high number of stars per solid angle, the Gaia telescope may have issues accurately measuring parallaxes and correctly identifying stars in this region. With this thought in mind, we check our radially separated results by cutting away the stars most likely to be biased by such an effect. Namely, we do this via three alternative methods: lowering our faintness cut to G < 17 mag, excising the GC via "box" cuts in l and b, and utilizing both of the aforementioned cuts in tandem.

For the first method, we see from Figure 9 that the two outermost radial bins do not change appreciably, which matches what one would expect given that the crowded regions of the sky do not subtend a large portion of the geometry there.

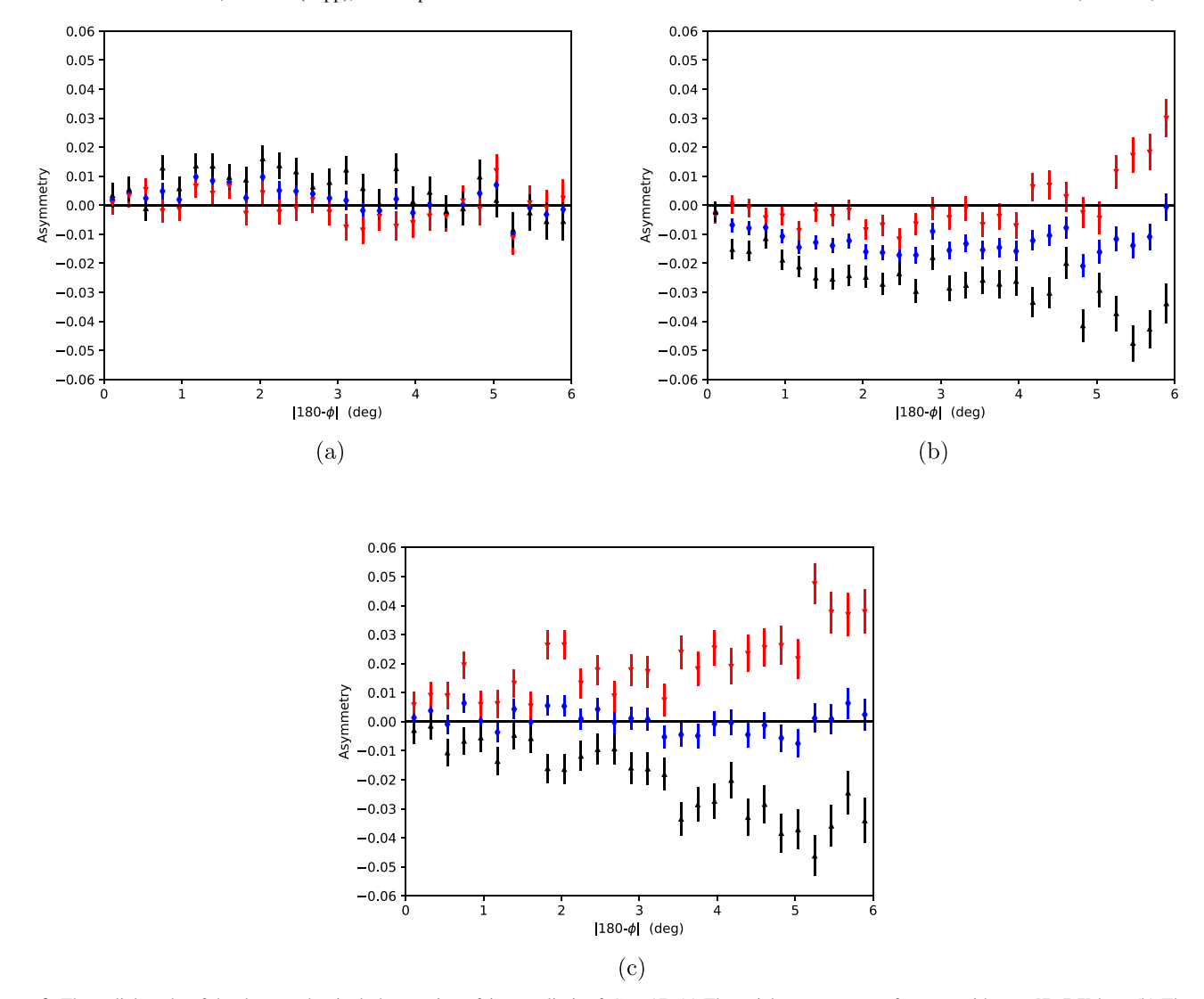


Figure 9. The radial study of the data set that includes a stricter faintness limit of G < 17. (a) The axial symmetry test for stars with $R \in [7, 7, 7]$ kpc. (b) The axial symmetry test for stars with $R \in [7, 7, 8.3]$ kpc. (c) The axial symmetry test for stars with $R \in [8.3, 9]$ kpc. Additional cuts used in all panels are: $0.5 < G_{\rm BP} - G_{\rm RP} < 2.5$ mag, 14 < G < 17 mag, $\varpi > 0$ mas, $|b| > 30^{\circ}$, 0.2 < |z| < 3.0 kpc, $|180^{\circ} - \phi| \le 6^{\circ}$, and the LMC/SMC excision outlined in Equations (2) and (3).

For the innermost R bin in panel (a), however, the GC is behind nearly all of the data. Minding the "hazy" G-band magnitude completeness limits of the Gaia telescope (Lindegren et al. 2018), we cut out the dimmest stars in order to test whether or not incompleteness affects the data. The north+south (blue diamonds) data do not change appreciably, while the north and south only curves become only slightly closer to zero.

For the second method, we choose to excise the densest region of the l, b plot in Figure 2(b). To wit, we cut out all stars within 20° of the l=0° line, which also satisfy |b|<45°. The results of this check are shown in Figure 10, where it is apparent that there is no appreciable change in any of the bins. Additionally, Figure 10(d) shows the altered xy footprint with the GC-masking l, b cuts employed.

For the third and final method of checking that our result is not appreciably afflicted by completeness and stellar identification issues in the dense GC region, we implement both the magnitude and "box" cuts mentioned above and show these results in Figure 11. Clearly, the largest R bin is unaffected by the l, b cuts and is identical to Figure 9(c). The intermediate R bin (Figure 11(b)) shows no appreciable change. Interestingly,

the innermost R bin appears to exhibit a wavelike north+south asymmetry, ⁴ a feature that was not as easily identifiable with the likely more poorly-measured GC-direction stars and dim stars included. Otherwise, the general trend remains mostly similar to the main result and the other tests.

2.7. Comparison of Stricter Cuts on the Aggregate Asymmetry Result

In order to assess if the additional cuts outlined in Section 2.6 appreciably change the resulting, aggregate asymmetry found in Gardner et al. (2020), we apply the same GC masking to the aggregate data set in Figure 12. Clearly, the results do not change qualitatively at all, and there is only a negligible quantitative change in the signal we find for each set of cuts. This fact allows us to conclude that potentially poorly

⁴ Although the asymmetries associated with innermost and outermost radial bins of Figure 11 appear to suggest wavelike features, a reduced chi-squared analysis reveals that Figure 11(a) contains the only statistically significant wavelike effect.

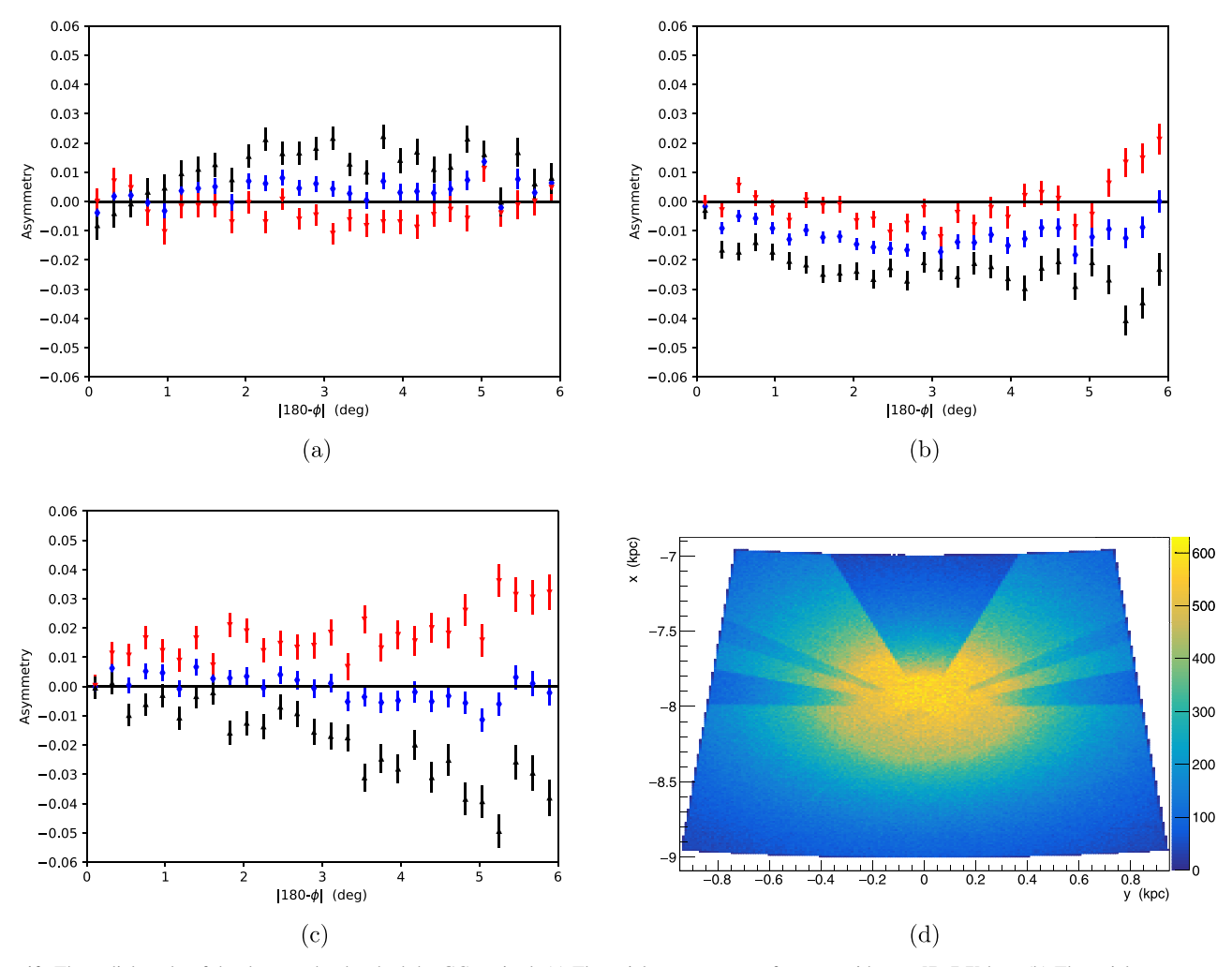


Figure 10. The radial study of the data set that has had the GC excised. (a) The axial symmetry test for stars with $R \in [7, 7.7]$ kpc. (b) The axial symmetry test for stars with $R \in [7.7, 8.3]$ kpc. (c) The axial symmetry test for stars with $R \in [8.3, 9]$ kpc is not affected by the GC excision and thus this is the same plot as Figure 8(c). (d) The xy footprint of the data when the GC excision is included. Additional cuts used in all panels are: $0.5 < G_{\rm BP} - G_{\rm RP} < 2.5$ mag, 14 < G < 18 mag, $\varpi > 0$ mas, $|b| > 30^{\circ}$, 0.2 < |z| < 3.0 kpc, $|180^{\circ} - \phi| \le 6^{\circ}$, and the LMC/SMC excision outlined in Equations (2) and (3).

measured stars in the denser regions of the sky near the GC are not responsible for the asymmetry we see.

2.8. Red and Blue Color Cut Analysis

Using only the nearest volume subset of our sample in order to isolate the color dependence (see Figure 13 caption for cuts), we see that the behavior of the red stars (Figure 13(a)) and the blue stars (Figure 13(b)) are both consistent with a downward trend in the north+south (blue diamonds) data, lending support to an overall distortion of the shape of the potential that is affecting all stars. There are, however, slight differences between the red and blue stars for the north–south data. This may be due to some effect seen only in the older, redder population, but we do not speculate on the specific cause.

2.9. Height Above the Plane Analysis

Finally, upon dividing the sample into subsets above and below |z| = 0.5 kpc, as in Figures 14(a)) and (b), respectively, one notices that the downward trend in the north+south data set (blue diamonds) appears to be much more marked for the low |z| stars, seemingly revealing behavior at odds with what one would expect if a distorted halo were the main cause of the

asymmetry. However, we have carefully removed the spiral arms via our b and z cuts. We note that the low-z stars preferentially sample the region of R close to the Sun due to the geometry of the latitude cuts imposed on the sample. Indeed, this behavior is completely consistent with a picture in which the OLR is inside the solar circle, as one would expect the low-|z| stars near $R=R_0$ to exhibit negative values of the asymmetry, due to the tendency of orbits to align with the bar just outside of the OLR (Binney & Tremaine 2008). In contrast, the more marked north—south difference for the high-|z| stars is consistent with a tilted prolate halo.

3. Results

As evident from Figures 12 and 8, our results do confirm the findings of Gardner et al. (2020), interpreted as an overall effect due to the LMC and SMC system, but also reveal *R*-dependent features. In particular, the sign flip in the asymmetry in Figure 8 as one looks closer to the GC suggests that another object contributes in that region. Given that the second most significant perturber noted by Gardner et al. (2020) is the Galactic bar, and that the signal occurs at smaller *R*, the Galactic bar is the most likely culprit.

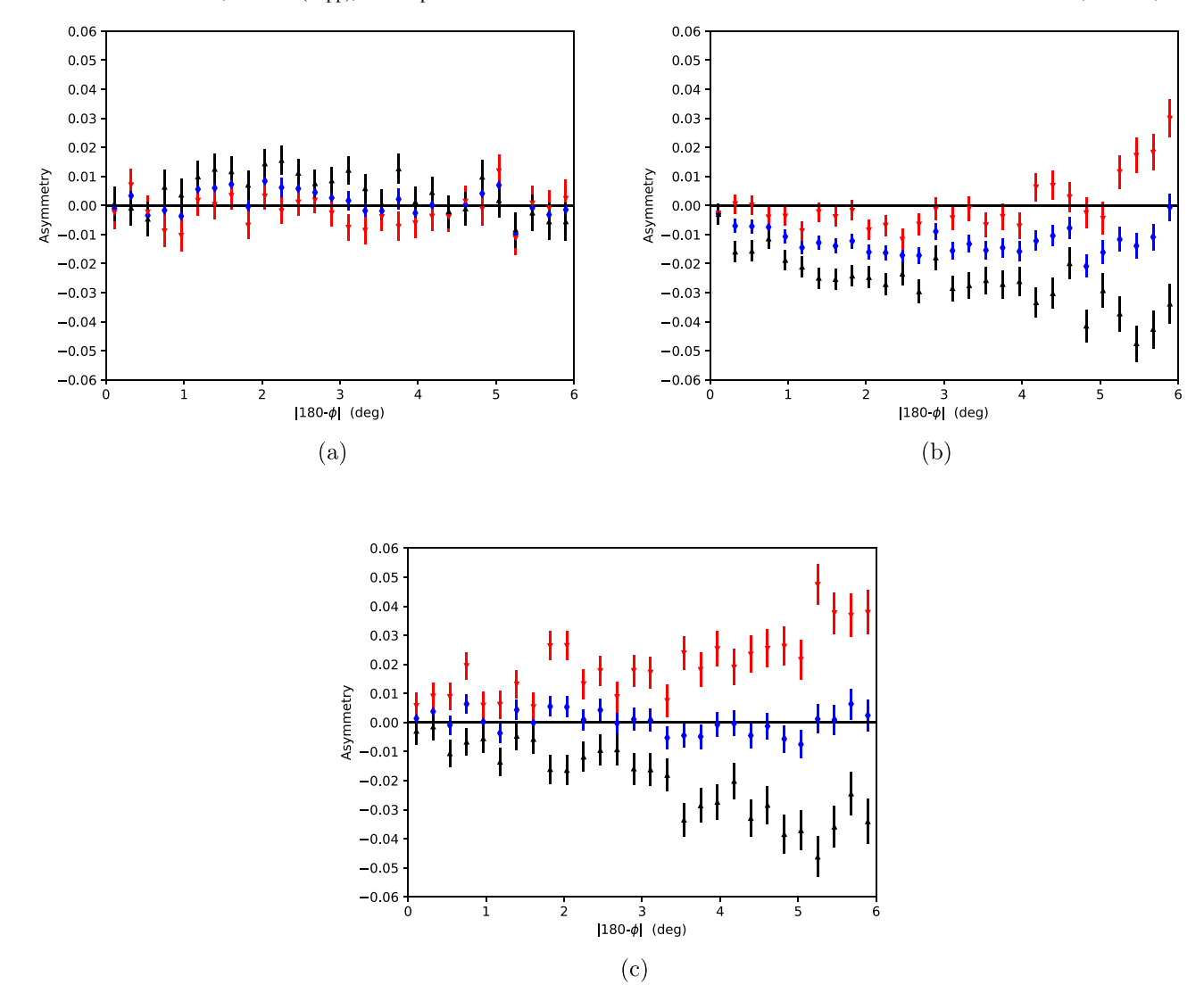


Figure 11. The radial study of the data set that includes a stricter faintness limit of G < 17 mag and the GC excision. (a) The axial symmetry test for stars with $R \in [7, 7.7]$ kpc. (b) The axial symmetry test for stars with $R \in [7, 7.7]$ kpc. (c) The axial symmetry test for stars with $R \in [8.3, 9]$ kpc is not affected by the GC excision and thus this is the same plot as Figure 9(c). Additional cuts used in all panels are: $0.5 < G_{\rm BP} - G_{\rm RP} < 2.5$ mag, 14 < G < 17 mag, $\varpi > 0$ mas, $|b| > 30^\circ$, 0.2 < |z| < 3.0 kpc, $|180^\circ - \phi| \le 6^\circ$, and the LMC/SMC excision outlined in Equations (2) and (3).

In fact, due to the nonaxisymmetric, time-dependent nature of the Galactic bar potential, resonances can occur at very specific Galactocentric radii (Binney & Tremaine 2008). While the existence of a family of stars in bar-resonant orbits depends strongly on the relative strength of the Galactic bar, it is the case for all but the strongest of bars that resonant orbits between the CR and the OLR orbit with trajectories perpendicular to the bar, and beyond the OLR the resonant orbits tend to be elongated along the bar's orientation (Contopoulos & Papayannopoulos 1980; Binney & Tremaine 2008). This non-axisymmetric behavior could easily be responsible for the sign flip we see in Figure 8, as there has long been a notion that a resonance occurs just interior to the solar circle (e.g., Mishurov & Zenina 1999; Dehnen 2000). Interestingly, given that the location of the Galactic bar is known, we believe that the pattern of axial asymmetries we see, that A flips sign from positive to negative, rather than from negative to positive, indicates that the effect is an OLR.

Finally, given the importance of Sgr in exciting vertical motions in the Galactic disk (Widrow et al. 2012; Yanny & Gardner 2013; Laporte et al. 2018), one might ask if it, too,

could have an effect axially on our sample. However, due to the alignment of the perturber and stars in our sample, the z-component of the torque would be very small, as the displacement vector and force vector are very nearly aligned, yielding a severely less significant torque. We expand upon the possible impact of the evolutionary history of the Sgr dwarf and stream below.

Thus the axial asymmetry profiles we have found appear consistent with two overarching effects: first, a matter distribution warped by the LMC and SMC, as suggested by the distorted halo model determined from studies of the Orphan stream by Erkal et al. (2019), and second, an asymmetry associated with an OLR driven by the Galactic bar.

In the distorted halo model, the dark halo of the Milky Way is stretched by the LMC/SMC system, causing an elongation in the direction of the Magellanic clouds (Erkal et al. 2019). With the Miyamoto-Nagai disk (Miyamoto & Nagai 1975) and distorted Navarro-Frenk-White halo profile (Navarro et al. 1997) of Erkal et al. (2019) integrated over the same region as our data set, the north only, south only, and north+south data sets all qualitatively match a reflex prolate distribution much

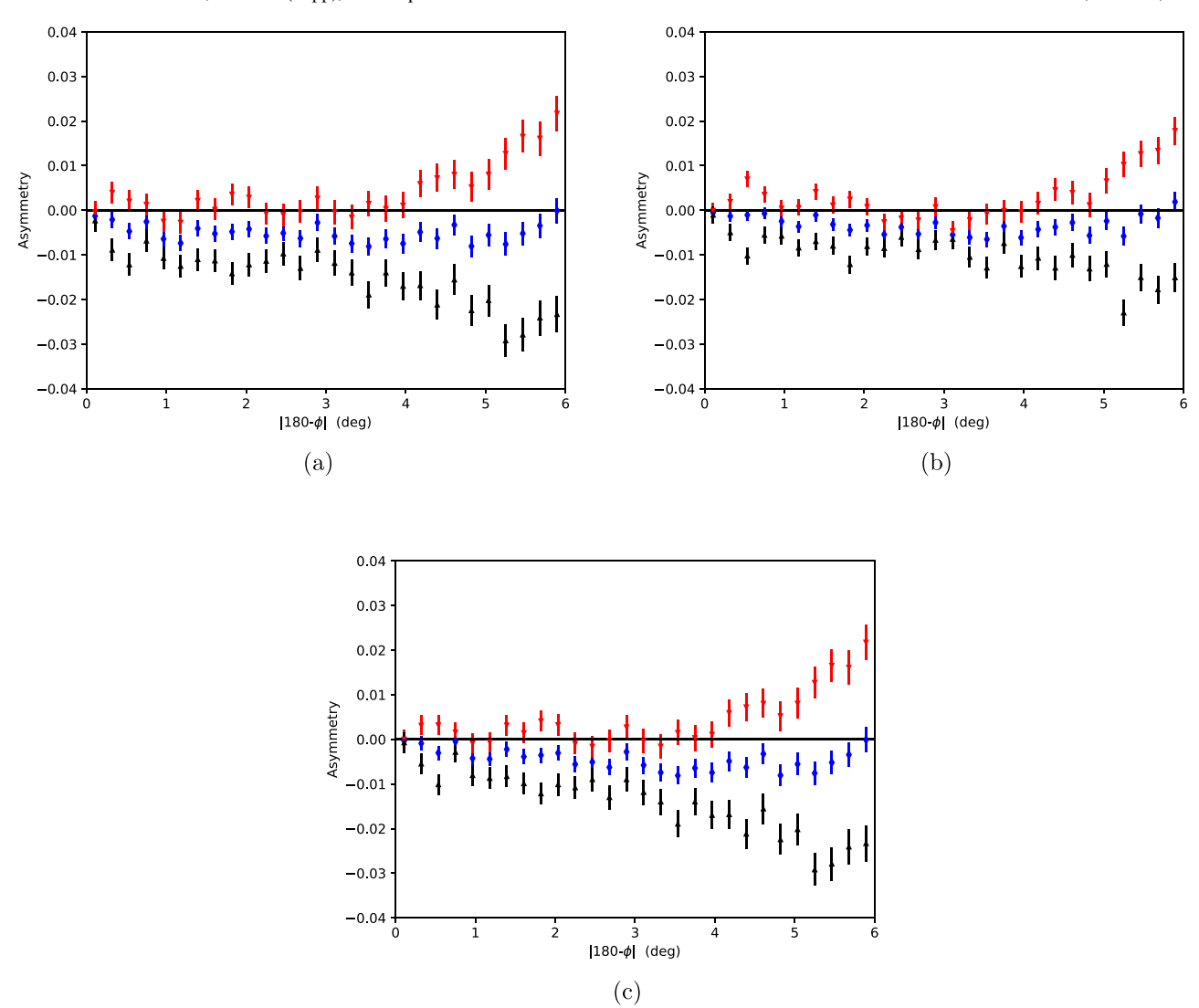


Figure 12. (a) Aggregate study of axial symmetry with G < 17 mag and the GC cuts of the above tests. (b) Aggregate study of axial symmetry from Gardner et al. (2020) with G < 18 mag. (c) The same as (b), but with G < 17 mag. Additional cuts used in all panels are: $0.5 < G_{\rm BP} - G_{\rm RP} < 2.5$ mag, $\varpi > 0$ mas, $|b| > 30^\circ$, 0.2 < |z| < 3.0 kpc, $|180^\circ - \phi| \le 6^\circ$, and the LMC/SMC excision outlined in Equations (2) and (3).

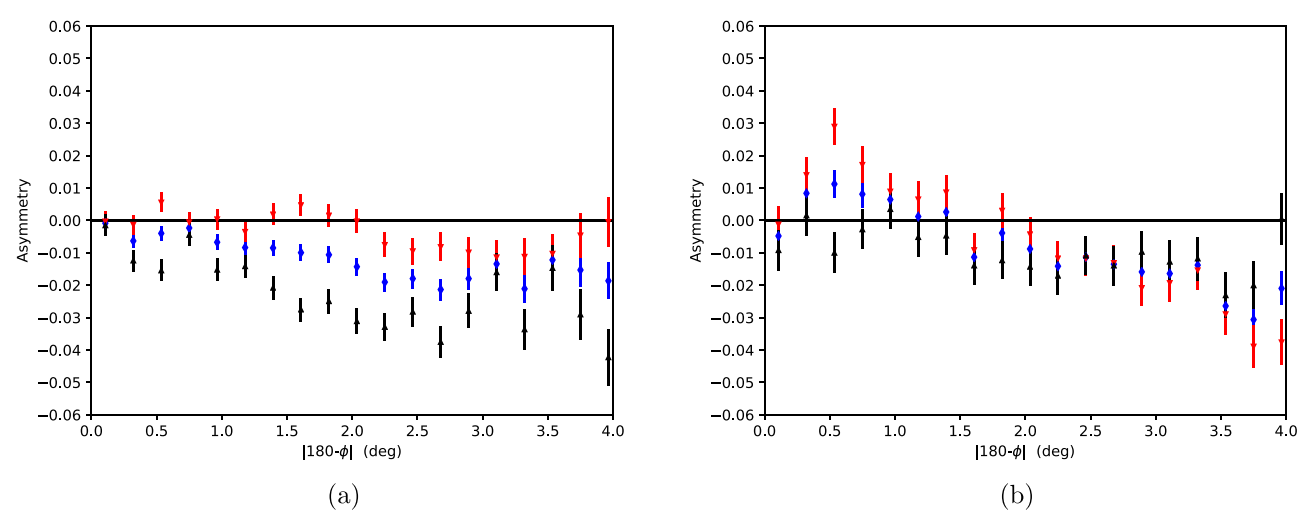
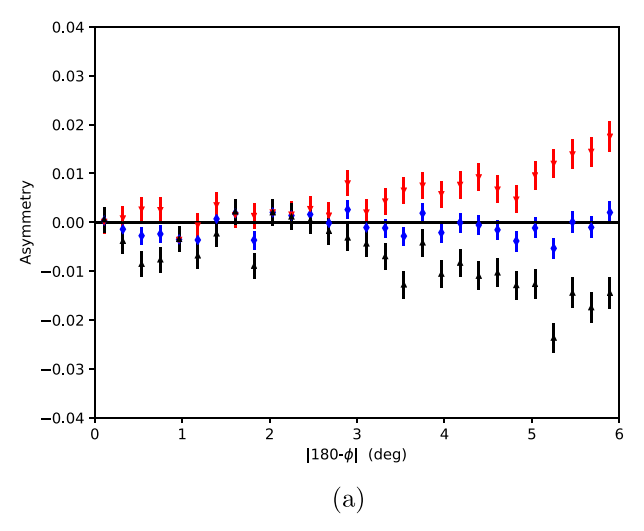


Figure 13. (a) Test of axial symmetry with red (1.5 < $G_{BP} - G_{RP} <$ 2.5 mag) stars only over a small volume of nearby space: 0.2 < |z| < 0.5 kpc and $R \in [7.5, 8.5]$ kpc. (b) Test of axial symmetry with blue (0.5 < $G_{BP} - G_{RP} <$ 1.5 mag) stars only over the same volume of space as (a). Additional cuts used in both panels are: $\varpi > 0$ mas, $|b| > 30^{\circ}$, $|180^{\circ} - \phi| \leqslant 4^{\circ}$, and the LMC/SMC excision outlined in Equations (2) and (3).



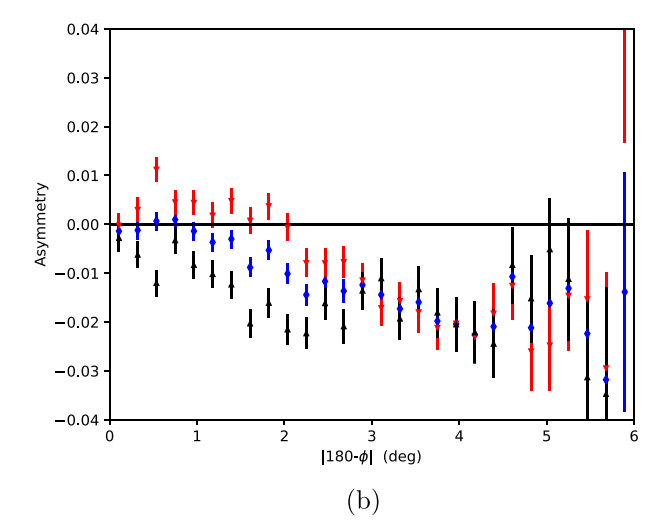


Figure 14. (a) Far from plane sample, 0.5 < |z| < 3 kpc. (b) Close to plane sample, 0.2 < |z| < 0.5 kpc. Additional cuts used in both panels are: $0.5 < G_{\rm BP} - G_{\rm RP} < 2.5$ mag, $\varpi > 0$ mas, $|b| > 30^\circ$, 7 < R < 9 kpc, $|180^\circ - \phi| \le 6^\circ$, and the LMC/SMC excision outlined in Equations (2) and (3). As the |b| cuts cause these panels to sample very different swaths of R, this figure does not show z-dependence alone. The low-z stars preferentially sample the region of R close to the Sun due to the geometry of the latitude cuts, which is consistent with the asymmetry expected from the region just beyond the OLR.

better than the other halo geometries offered (Gardner et al. 2020). As we have mentioned in Gardner et al. (2020), this halo geometry is also consistent with the Galactic warp picture of Weinberg & Blitz (2006) and Dekel & Shlosman (1983).

It is perhaps disconcerting, though, that upon dividing the data set into radial or vertical bins, the allegedly global asymmetry effect of a distorted matter distribution is not seen at the same level in each bin. Indeed, the vertical-axial correlation and north+south trend of Figure 8(a) is reversed from what is expected, while panels (b) and (c) still fit well with this picture. Additionally, as can be seen from Figure 14 the axial asymmetry is largely seen in stars close to the plane, the opposite of what one would expect for a halo-driven effect. However, due to the nature of the |b| cuts implemented here, different bands of |z| sample different values of R, as can be understood from Figure 7(b). Thus, it is possible that the zdependence is confounded by sampling different values of R. Regardless, the picture of Magellanic Cloud influence alone cannot explain the innermost R bin, and thus requires some additional effect. This effect is likely from the Galactic bar as it is only seen at the innermost R bin. Indeed we believe it to be the result of the presence of the OLR. This effect, believed to be just inside the solar circle (Dehnen 2000), can cause perturbations to stars just inside (outside) the OLR that cause them to align themselves in a perpendicular (parallel) sense with respect to the bar (Contopoulos & Papayannopoulos 1980; Dehnen 2000). Given that the Galactic Bar is known to point at approximately 13°-27° from the Sun's location (Robin et al. 2012; Portail 2016), this orbital alignment configuration would give rise to an axial asymmetry that is left heavy (A > 0) for values of R just inside the OLR, and right heavy (A < 0) for values of R just outside the OLR, and no net effect well beyond the OLR. This qualitatively matches the results of Figure 8. Note that if the effect were a CR, the asymmetry ought to flip from negative to positive.

It is unclear exactly how the stars near the OLR can behave in such a way to also cause a north-south asymmetry, but it has been noted that the vertical resonance from a central bar can have significant effects on the vertical amplitudes of orbits near the Inner Lindblad Resonance (Hasan et al. 1993; Quillen 2002), so that such an effect near the OLR could well also occur.

Upon consideration of the above effects, it seems most likely that both a Magellanic torque and bar-induced resonances are operative on the local star count data. The OLR creates a left-heavy asymmetry in the innermost R bin and constructively interferes with the LMC- and SMC-driven (halo) effect in the middle R bin. Finally, the OLR ceases to play a large role at higher R and the halo effect is the lone cause of the signal we see.

We have determined the location of the in-plane radius at which the axial asymmetry, north+south, flips sign as follows. We compute the asymmetry $\langle \mathcal{A}(\phi) \rangle$, making an error-weighted average over azimuthal angles such that $|180^{\circ} - \phi| < 6^{\circ}$, where $\mathcal{A}(\phi)$ itself counts up stars in a wedge of width ΔR , for various choices of starting radius R_i . We refine the determined radius at which $\langle \mathcal{A}(\phi) \rangle$ flips sign through an iterative procedure. That is, we begin with wedges of width $\Delta R = 500$ pc and move outward in R_i by 200 pc increments to determine where the average asymmetry changes sign. After observing a sign flip, the radial width of each bin is decreased, and the scan repeated over a smaller range of R_i to sharpen the determination of the radial location of the sign flip. The uncertainty is derived from the smallest radial wedge, of 200 pc, that still reveals a sign flip in the asymmetry at a magnitude larger than the combined uncertainty in $|\langle \mathcal{A}(\phi) \rangle|$, where the statistical error in $\langle \mathcal{A}(\phi) \rangle$ and the systematic error $|A_{\rm sys}| = 0.0009$ have been combined in quadrature. Noting Table 2, and picking the midpoint of the $R_i - R_f$ bin with the smallest asymmetry for a ΔR of 200 pc we have determined that $R_{\rm flip} = (0.95 \pm 0.03)~R_0$. Our sign flip analysis uses the data set of Gardner et al. (2020) and implicitly assumes that only one effect is operative in the data. However, we also expect the distorted halo to make some contribution as an overall negative offset to the asymmetry. This offset, determined at larger R, is small and implies $R_{\rm OLR} > R_{\rm flip}$. This effect, as well as other refinements in our determination of $R_{\rm OLR}$, and its implications, we plan to analyze in a future paper (A. Hinkel et al. 2020, in preparation).

The OLR picture allows for a number of follow-up studies. First, if the OLR is responsible for the behavior we observe at

Table 2
Asymmetry Sign Flip Analysis

$R_i - R_f \text{ (kpc)}$	ΔR (kpc)	$\langle \mathcal{A}(\phi) \rangle$	$\sigma_{\langle \mathcal{A} angle}$	Sign
7.0–7.5	0.5	+0.0071	0.0012	+
7.2-7.7	0.5	+0.0035	0.0011	+
7.4-7.9	0.5	-0.0027	0.0011	_
7.3–7.6	0.3	+0.0049	0.0012	+
7.4–7.7	0.3	+0.0017	0.0012	+
7.5–7.8	0.3	-0.0019	0.0012	_
7.45-7.65	0.2	+0.0030	0.0013	+
7.5–7.7	0.2	+0.0005	0.0013	+
7.55–7.75	0.2	-0.0019	0.0012	_

Note. Axial asymmetries, north+south, averaged over azimuth angles about the anticenter direction up to $|180^{\circ} - \phi| = 6^{\circ}$, computed for a wedge of size ΔR for different choices of starting radius R_i , with $R_f = R_i + \Delta R$, to reveal the sign change in the average asymmetry as $R_i - R_f$ changes. We refine the location of the sign flip iteratively by computing the average asymmetry with R_i for smaller ΔR .

smaller R, we should be able to connect the asymmetry to a radial velocity difference between stars on the left and right of the $\phi=180^\circ$ line. Studying the axial asymmetry about values of ϕ other than $\phi=180^\circ$ could also be revealing, as the stellar orbits just within and beyond the OLR have crossing points in ϕ . Moreover, in this picture we would also not expect to find significant variation of the axial asymmetry with R beyond the Sun's location, which we hope to investigate further, including with the upcoming Gaia DR3 data set.

Finally, we consider whether past effects of the Sgr dwarf galaxy's collision with the Milky Way could cause an appreciable signal in our data set. Since the mass used in Gardner et al. (2020) referred to the present day core of the Sgr dwarf spheroidal, it is interesting to ask if its more massive past self (estimated by Purcell et al. 2011 to have a mass of roughly $10^{10.5}$ – $10^{11}M_{\odot}$) could torque the disk appreciably. While it is true that Sgr would have applied a significant torque on the Galaxy, the axial dispersion velocities of approximately 30 km s⁻¹ (Purcell et al. 2011) ensure that any asymmetry incurred from the original impact before the significant mass losses of nearly 2 Gyr ago (Purcell et al. 2011) will have been diluted to cover an arc over 50 times larger, reducing the magnitude of any axial asymmetry signal to irrelevance for our volume of space in the present time. That the vertical motions of stars can be affected by Sgr, suggested in Widrow et al. (2012), Yanny & Gardner (2013), and Ferguson et al. (2017) is an entirely different matter.

With regard to the possible influence of the Sgr dwarf tidal stream of the present day we note that a recent impact of Sgr with the disk is very perpendicular to the plane of the disk and at roughly $\phi \approx 180^\circ$, thus giving, as we have noted, nearly zero azimuthal torque on the stars in our sample. This leads us to argue that the LMC, while at a significantly greater distance from the Sun than the Sgr tidal stream, induces a much larger left-right asymmetry than Sgr (or the bar if $R \lesssim 8$ kpc).

4. Conclusions

We support and expand upon the findings of Gardner et al. (2020) regarding the existence and origin of axial asymmetries in star counts, strongly correlated with mass density in the solar neighborhood, using the Gaia DR2 data set. After making appropriately conservative cuts, we arrive at a complete,

distance-error limited sample of stars, in matched left-right and north-south volumes, that shows residual asymmetries in the counts of between 0.5% and 3%. We explore and rule out possible incompleteness due to reddening, lines of sight polluted by regions of high stellar density, significant errors in parallax, magnitude and color limits, and other geometric cuts. Based on the estimated azimuthal torques applied to density in the solar neighborhood from Galactic and Local Group structure, we isolate the Magellanic Cloud system as capable of inducing the largest asymmetry for radii $7.7 < R < 9 \,\mathrm{kpc}$, as shown in Gardner et al. (2020). Recent increases in mass estimates for the LMC and SMC system (Erkal et al. 2019) give this perturber an outsized influence, compared with earlier estimates. Going beyond Gardner et al. (2020), subdividing the data into three radial bins, we note that the lowest radial bin, 7 < R < 7.7 kpc, exhibits a sign flip in the asymmetry incompatible with the Magellanic Cloud influence, but consistent with that expected from a bar-induced OLR located slightly beyond $R = 7.6 \,\mathrm{kpc}$ ($R_{\mathrm{flip}} = (0.95 \pm$ (0.03) (R_0) . While a detailed model that includes several perturbers simultaneously and that considers reflex backreaction is needed to fully model the detailed asymmetries seen here, we have demonstrated the potential for precision studies of symmetry breaking to constrain and inform our knowledge of the overall mass distribution in and around our Milky Way.

A.H. thanks the Universities Research Association and the GAANN fellowship for funding. S.G. and A.H. acknowledge partial support from the U.S. Department of Energy under contract DE-FG02-96ER40989. We also thank the anonymous referee of Gardner et al. (2020) for helpful insights, which strengthened the investigation of systematics, and thank the anonymous referee of this paper for helpful comments that improved the quality of this work.

This document was prepared in part using the resources of Fermi National Accelerator Laboratory (Fermilab), a U.S. Department of Energy, Office of Science, HEP User Facility. Fermilab is managed by the Fermi Research Alliance, LLC (FRA), acting under Contract No. DE-AC02-07CH11359.

This work has made use of data from the European Space Agency (ESA) mission Gaia (https://www.cosmos.esa.int/gaia), processed by the Gaia Data Processing and Analysis Consortium (DPAC, https://www.cosmos.esa.int/web/gaia/dpac/consortium). Funding for the DPAC has been provided by national institutions, in particular the institutions participating in the Gaia Multilateral Agreement.

ORCID iDs

Austin Hinkel https://orcid.org/0000-0002-9785-914X Susan Gardner https://orcid.org/0000-0002-6166-5546 Brian Yanny https://orcid.org/0000-0002-9541-2678

References

Abuter, R., Amorim, A., Bauböck, M., et al. 2019, A&A, 625, L10 Arenou, F., Luri, X., Babusiaux, C., et al. 2018, A&A, 616, A17 Bailer-Jones, C. A. 2015, PASP, 127, 994 Bennett, M., & Bovy, J. 2018, MNRAS, 482, 1417 Binney, J. 2012, MNRAS, 426, 1324 Binney, J. 2019, arXiv:1909.02455 Binney, J., Burnett, B., Kordopatis, G., et al. 2014, MNRAS, 439, 1231 Binney, J., & Piffl, T. 2015, MNRAS, 454, 3653

```
Binney, J., & Tremaine, S. 2008, Galactic Dynamics (Princeton, NJ: Princeton
  Univ. Press)
Bovy, J., & Rix, H.-W. 2013, ApJ, 779, 115
Contopoulos, G., & Papayannopoulos, T. 1980, A&A, 92, 33
Dehnen, W. 2000, AJ, 119, 800
Dekel, A., & Shlosman, I. 1983, in IAU Symp. 100, Internal Kinematics and
   Dynamics of Galaxies, ed. E. Athanassoula (Dordrecht: D. Reidel), 187
Erkal, D., Belokurov, V., Laporte, C., et al. 2019, MNRAS, 487, 2685
Ferguson, D., Gardner, S., & Yanny, B. 2017, ApJ, 843, 141
Gardner, S., Hinkel, A., & Yanny, B. 2020, ApJ, 890, 110
Hasan, H., Pfenniger, D., & Norman, C. 1993, ApJ, 409, 91
Jeans, J. H. 1915, MNRAS, 76, 70
Laporte, C. F., Johnston, K. V., Gómez, F. A., Garavito-Camargo, N., &
   Besla, G. 2018, MNRAS, 481, 286
Lindegren, L., Hernandez, J., Bombrun, A., et al. 2018, A&A, 616, A2
Lindegren, L., Lammers, U., Hobbs, D., et al. 2012, A&A, 538, A78
Luri, X., Brown, A., Sarro, L., et al. 2018, A&A, 616, A9
Michalik, D., Lindegren, L., Hobbs, D., & Butkevich, A. G. 2015, A&A,
   583, A68
Mishurov, Y. N., & Zenina, I. 1999, A&A, 341, 81
Miyamoto, M., & Nagai, R. 1975, PASJ, 27, 533
```

```
Mróz, P., Udalski, A., Skowron, D. M., et al. 2019, ApJL, 870, L10
Navarro, J. F., Frenk, C. S., & White, S. D. 1997, ApJ, 490, 493
Noether, E. 1918, Nachr. v. d. Ges. d. Wiss. Zu Göttingen, 235
Olver, P. J. 1993, Applications of Lie Groups to Differential Equations (2nd
  ed.; Berlin: Springer)
Piffl, T., Binney, J., McMillan, P. J., et al. 2014, MNRAS, 445, 3133
Piffl, T., Penoyre, Z., & Binney, J. 2015, MNRAS, 451, 639
Portail, M. 2016, PhD thesis, LMU München
Prusti, T., De Bruijne, J., Brown, A. G., et al. 2016, A&A, 595, A1
Purcell, C. W., Bullock, J. S., Tollerud, E. J., Rocha, M., & Chakrabarti, S.
  2011, Natur, 477, 301
Quillen, A. C. 2002, AJ, 124, 722
Robin, A. C., Marshall, D. J., Schultheis, M., & Reylé, C. 2012, A&A,
   538, A106
Robin, A. C., Reylé, C., Derriere, S., & Picaud, S. 2003, A&A, 409, 523
Stassun, K. G., & Torres, G. 2018, arXiv:1805.03526
Weinberg, M. D., & Blitz, L. 2006, ApJL, 641, L33
Widrow, L. M., Gardner, S., Yanny, B., Dodelson, S., & Chen, H.-Y. 2012,
   ApJL, 750, L41
Yanny, B., & Gardner, S. 2013, ApJ, 777, 91
Zinn, J. C., Pinsonneault, M. H., Huber, D., & Stello, D. 2019, ApJ, 878, 136
```